

## Hyperbolic plasmon modes in tilted Dirac cone phases of borophene

Zahra Torbatian,<sup>1</sup> Dino Novko<sup>2,3,\*</sup> and Reza Asgari<sup>4,5,6,†</sup>

<sup>1</sup>*School of Nano Science, Institute for Research in Fundamental Sciences (IPM), Tehran 19395-5531, Iran*

<sup>2</sup>*Institute of Physics, Zagreb 10000, Croatia*

<sup>3</sup>*Donostia International Physics Center (DIPC), Donostia-San Sebastián 20018, Spain*

<sup>4</sup>*School of Physics, Institute for Research in Fundamental Sciences (IPM), Tehran 19395-5531, Iran*

<sup>5</sup>*School of Physics, University of New South Wales, Kensington, NSW 2052, Australia*

<sup>6</sup>*ARC Centre of Excellence in Future Low-Energy Electronics Technologies, UNSW Node, Sydney 2052, Australia*

 (Received 23 June 2021; revised 6 August 2021; accepted 10 August 2021; published 18 August 2021)

Hyperbolic materials are receiving significant attention due to their ability to support electromagnetic fields with arbitrarily high momenta and, hence, to achieve very strong light confinement. Here, based on first-principles calculations and many-body perturbation theory, we explore the characteristic of two-dimensional plasmon modes and its hyperbolic properties for two phases of single-layer boron hosting tilted Dirac cone, namely, the *hr-sB* and *8Pmmn* borophene. In-plane anisotropy in borophene is manifested in the structural, electronic, vibrational, and optical properties. We find two hyperbolic regimes for both phases of borophene, where the high-energy one is located in the visible range. The *hr-sB* borophene is characterized with an intrinsic high carrier density and it supports strong hyperbolic plasmon modes in the visible part of the spectrum. The *8Pmmn* borophene, on the other hand, resembles the prototypical Dirac material graphene and on carrier doping acquires anisotropic Dirac plasmons in the mid-infrared. We have also investigated the impact of the electron-phonon coupling and Landau damping on these hyperbolic plasmon modes. Our results show that borophene, having high anisotropy, intrinsic high carrier concentration, low-loss hyperbolic Dirac plasmon modes, and high confinement can represent a promising candidate for low-loss broadband surface plasmon polariton devices.

DOI: [10.1103/PhysRevB.104.075432](https://doi.org/10.1103/PhysRevB.104.075432)

### I. INTRODUCTION

Natural hyperbolic materials, with anisotropic dielectric constants where the real parts of the principle components have opposite signs, have recently attracted much attention [1–6]. These materials support electromagnetic modes with large wave vectors and exhibit directionally propagating polaritons with extremely large photonic density of states (DOS) [2,7–9]. Polaritons in natural materials can be formed when the light interacts with the intrinsic plasmons, phonons, or excitons [10,11]. In contrast to the artificial metasurfaces, where hyperbolic dispersion is limited to wave vectors smaller than the inverse of the structure size, natural hyperbolic materials support high electromagnetic confinement and contain no internal interfaces for the electrons to scatter off [2]. Naturally occurring hyperbolic plasmonic media are rare, and thus far they were experimentally verified to exist only in the WTe<sub>2</sub> thin film [12,13]. However, recent theoretical studies have predicted attractive hyperbolic properties not only in WTe<sub>2</sub> [14] but also in black phosphorous [8,15,16], cuprates, MgB<sub>2</sub> [2], electrides [17], MoTe<sub>2</sub> [18,19], layered hexagonal crystal structures [20], and MoOCl<sub>2</sub> [21]. In most cases, ideal natural hyperbolic plasmonic material is required to possess

high structural and electronic anisotropy, high carrier density, and low plasmonic losses. Here we propose two phases of borophene with such electronic and optical properties that might be naturally suitable to serve as an efficient hyperbolic plasmonic material.

Recently, two-dimensional (2D) boron with high free charge carrier concentration emerged as a perfect 2D metal with extraordinary electric, optical, and transport properties [22–31]. In fact, borophene, as an intrinsic 2D metal with both high carrier density and high confinement, can be a promising candidate for optical devices based on low-loss broadband surface plasmon polaritons [29,31]. Until now, a number of monolayer boron sheets have been theoretically predicted and three types of borophene fabricated in the experiment, i.e., strip,  $\beta_{12}$ , and  $\chi_3$  borophene [32,33].

In this paper, we investigate two phases of borophene, namely, *8Pmmn* and *hr-sB*. The first one represents a polymorph of borophene that hosts an anisotropic tilted Dirac cone [34–37]. The Dirac cone was thus far confirmed to exist in the  $\beta_{12}$  phase of borophene on Ag(111) [38] and indicated in reconstructed borophene polymorph on Ir(111) [39]. The second one, i.e., *hr-sB*, is a newly predicted boron monolayer with two types of Dirac fermions coexisting in the sheet; one type is related to Dirac nodal lines and the other is related to tilted semi-Dirac cones with strong anisotropy. This new allotrope possesses a high stability compared with the experimentally available  $\delta_6$ ,  $\beta_{12}$ , and  $\chi_3$  sheets [40]. Here

\*dino.novko@gmail.com

†asgari@ipm.ir

we investigate characteristics of 2D Dirac plasmons and its hyperbolic properties for these two phases of borophene in the framework of density functional theory (DFT) and many-body perturbation theories. Our results show that both phases of borophene support strong Dirac hyperbolic plasmons due to their highly anisotropic optical properties. Owing to the high intrinsic carrier concentration, hyperbolic Dirac plasmons in the *hr-sB* borophene are present also in the visible range. In addition, we explore the coupling of Dirac plasmons with phonons as well as with the electron-hole pairs from first principles. This allows us to study the decay rates of plasmons in borophene and assess its efficiency both qualitatively and quantitatively. Interestingly, we find extremely negligible plasmonic losses in the *8Pmmn* borophene, which are actually comparable to the losses in prototypical Dirac material graphene. Therefore, these novel 2D hyperbolic Dirac materials are promising and appealing for applications in plasmonics.

This paper is organized as follows. The theory and computational details are presented in Sec. II where we discuss the optical absorption, phonon-induced damping, and electron excitation spectrum in the system. Our numerical results and discussions are given in Sec. III demonstrating the electron band structure and hyperbolic optical features of monolayer borophene systems. Our main results are summarized in Sec. IV.

## II. THEORY AND COMPUTATIONAL METHODS

Our first-principles calculations are based on the DFT within the Quantum ESPRESSO package [41] using Perdew-Zunger functional for exchange-correlation functional. The plane-wave energy cutoff is fixed to 50 Ry. The 2D layers are modeled in periodic cells with 20 Å vacuum in the direction normal to the layer to reduce the interaction between periodic images. The convergence criterion for energy is set to  $10^{-8}$  eV and the atomic positions are relaxed until the Hellmann-Feynman forces are less than  $10^{-4}$  eV/Å. The 2D Brillouin zone (BZ) is sampled using  $48 \times 24 \times 1$  and  $30 \times 40 \times 1$  k-point meshes for the *hr-sB* and *8Pmmn* phases of borophene, respectively. To accurately determine the electron-phonon coupling (EPC) constants, we employed recently developed Wannier interpolation technique [42], which has been implemented in the EPW code [43]. To do so, the electronic structure, dynamical matrices, and electron-phonon matrix elements obtained from DFT and density functional perturbation theory (DFPT) [44] were used as the initial data for Wannier interpolation within the maximally localized Wannier functions formalism.

### A. Optical absorption, phonon-induced damping, and electron excitation spectrum

In this section, we present a brief theoretical description of optical absorption quantities in the long-wavelength limit ( $\mathbf{q} \approx 0$ ) by making use of the current-current response tensor  $\Pi_\mu(\mathbf{q}, \omega)$  calculated within DFT, where the electromagnetic interaction is mediated by the free-photon propagator. The thorough description of the method can be found in our previous works [45–47].

The optical conductivity can be calculated as  $\sigma_\mu(\omega) = -i \lim_{\mathbf{q} \rightarrow 0} \Pi_\mu^0(\mathbf{q}, \omega)/\omega$ , while the optical absorption is given by  $A(\mathbf{q}, \omega) = -4\hbar \text{Im} \Pi_\mu(\mathbf{q}, \omega)/\omega$  [45,46,48], where  $\Pi_\mu^0(\mathbf{q}, \omega)$  is a bare current-current tensor, while  $\Pi_\mu(\mathbf{q}, \omega)$  is a fully screened tensor.

To investigate the effects of phonons on the plasmon dispersion, we implement the formalism presented in Refs. [48,49]. Optical excitations are first convenient to decompose into the intraband ( $n = m$ ) and interband ( $n \neq m$ ) contributions, i.e.,  $\Pi_\mu^0 = \Pi_\mu^{0,\text{intra}} + \Pi_\mu^{0,\text{inter}}$ . The electron-phonon scattering mechanism is then considered in the intraband channel.

In the optical limit when  $\mathbf{q} \approx 0$ , the noninteracting interband current-current response tensor is

$$\Pi_\mu^{0,\text{inter}}(\omega) = \frac{2}{V} \sum_{\mathbf{k}, n \neq m} \frac{\hbar\omega}{E_n(\mathbf{k}) - E_m(\mathbf{k})} \times |J_{nm\mathbf{k}}^\mu|^2 \frac{f_n(\mathbf{k}) - f_m(\mathbf{k})}{\hbar\omega + i\eta + E_n(\mathbf{k}) - E_m(\mathbf{k})}, \quad (1)$$

where  $J_{nm\mathbf{k}}^\mu$  are the current vertices,  $E_n(\mathbf{k})$  are the Kohn-Sham energies,  $f_n(\mathbf{k})$  is the Fermi-Dirac distribution function at temperature  $T$ ,  $\mu$  are the polarization directions, and  $V$  is the normalized volume. Further, the summation over  $\mathbf{k}$  wave vectors is carried on a  $200 \times 70 \times 1$  ( $180 \times 240 \times 1$ ) grid for *hr-sB* (*8Pmmn*) phase of borophene,  $n$  band index sums over 30 electronic bands.

The corresponding intraband contribution of current-current response tensor can be written as the following [48,50]:

$$\Pi_\mu^{0,\text{intra}}(\omega) = \frac{2}{V} \frac{\omega}{\omega[1 + \lambda_{\text{ph}}(\omega)] + i/\tau_{\text{ph}}(\omega)} \sum_{\mathbf{k}, n} \frac{\partial f_{nk}}{\partial E_{nk}} |J_{nk}^\mu|^2. \quad (2)$$

Here the effects of the EPC are contained in the temperature-dependent dynamical scattering time and energy renormalization parameters, i.e.,  $\tau_{\text{ph}}(\omega)$  and  $\lambda_{\text{ph}}(\omega)$ , respectively. The dynamical scattering time is given by [51,52]

$$\hbar/\tau_{\text{ph}}(\omega) = \frac{\pi\hbar}{\omega} \int d\Omega \alpha^2 F(\Omega) \left[ 2\omega \coth \frac{\Omega}{2k_B T} - (\omega + \Omega) \coth \frac{\omega + \Omega}{2k_B T} + (\omega - \Omega) \coth \frac{\omega - \Omega}{2k_B T} \right], \quad (3)$$

where  $k_B$  is the Boltzmann constant and  $\alpha^2 F(\Omega)$  is the Eliashberg spectral function [48,49]

$$\alpha^2 F(\omega) = \frac{1}{2\pi N(e_F)} \sum_{\mathbf{q}\nu} \delta(\omega - \omega_{\mathbf{q}\nu}) \frac{\gamma_{\mathbf{q}\nu}}{\hbar\omega_{\mathbf{q}\nu}}, \quad (4)$$

in which  $\omega_{\mathbf{q}\nu}$  and  $\gamma_{\mathbf{q}\nu}$  are the frequency and linewidth for phonon mode  $\nu$  at wave vector  $\mathbf{q}$ ;  $N(e_F)$  is the DOS at the Fermi level. Finally, the dynamical energy renormalization parameter  $\lambda_{\text{ph}}(\omega)$  is obtained by performing the Kramers-Kronig transformation of  $1/\tau_{\text{ph}}(\omega)$ .

The total EPC constant can be determined by either BZ summation or the frequency-space integration:

$$\lambda = \sum_{\mathbf{q}\nu} \lambda_{\mathbf{q}\nu} = 2 \int \frac{\alpha^2 F(\omega)}{\omega} d\omega, \quad (5)$$

where  $\lambda_{\mathbf{q}\nu}$  is the mode- and momentum-resolved EPC constant. Notice that the phonon properties (i.e., phonon energies and electron-phonon matrix elements) needed for calculating  $\alpha^2 F(\omega)$  are obtained within the EPW code [43]. The calculations of the EPC constants and Eliashberg function are performed on dense grids of  $400 \times 200$  ( $120 \times 160$ )  $\mathbf{k}$ - and  $80 \times 40$  ( $30 \times 40$ )  $\mathbf{q}$ -points for *hr-sB* ( $8Pmnn$ ) phase of borophene, which ensures the numerical convergence of the results presented in this work. Having considered these results, we can calculate the scattering rate by using Eq. (3) and finally the phonon-induced plasmon decay for both phases of borophene.

The electronic excitation spectra within the random-phase approximation (RPA) for finite momentum ( $\mathbf{q} > 0$ ) are calculated by means of charge-charge correlation function formalism. The dielectric function in the RPA is given by

$$\varepsilon_{\mathbf{G}\mathbf{G}'}(\mathbf{q}, \omega) = \delta_{\mathbf{G}\mathbf{G}'} - \sum_{\mathbf{G}_1} v_{\mathbf{G}\mathbf{G}_1}(\mathbf{q}) \chi_{\mathbf{G}_1\mathbf{G}'}^0(\mathbf{q}, \omega), \quad (6)$$

where the charge-charge correlation function is given by

$$\chi_{\mathbf{G}\mathbf{G}'}^0(\mathbf{q}, \omega) = \frac{2}{V} \sum_{\mathbf{k}, m, m'} \frac{f_m(\mathbf{k}) - f_{m'}(\mathbf{k} + \mathbf{q})}{\hbar\omega + i\eta + E_n(\mathbf{k}) - E_{m'}(\mathbf{k} + \mathbf{q})} \times M_{n\mathbf{k}, m\mathbf{k} + \mathbf{q}}(\mathbf{G}) M_{n\mathbf{k}, m\mathbf{k} + \mathbf{q}}^*(\mathbf{G}'). \quad (7)$$

Here  $\mathbf{G}$  is the reciprocal lattice wave vector and  $v_{\mathbf{G}\mathbf{G}'}$  is the bare Coulomb interaction. The charge matrix elements are defined as

$$M_{n\mathbf{k}, m\mathbf{k} + \mathbf{q}}(\mathbf{G}) = \langle \psi_{n\mathbf{k}} | e^{-i(\mathbf{q} + \mathbf{G})\mathbf{r}} | \psi_{m\mathbf{k} + \mathbf{q}} \rangle_V, \quad (8)$$

where  $\psi_{n\mathbf{k}}(\mathbf{r})$  are Kohn-Sham wave functions. The electron energy loss spectrum is obtained by calculating

$$\text{EELS} = -\text{Im}[1/\varepsilon_{\mathbf{G}\mathbf{G}'}(\mathbf{q}, \omega)]_{\mathbf{G}=\mathbf{G}'=0}, \quad (9)$$

which, in addition, contains plasmon poles at  $\hbar\omega_{\text{pl}}$  as well as the screened interband and intraband excitations. The corresponding calculations are performed within the GPAW [53] code using the PAW pseudopotentials with energy cutoff of 600 eV, LDA functional, and a  $30 \times 20 \times 1$  ( $20 \times 30 \times 1$ ) electron-momentum grid for *hr-sB* ( $8Pmnn$ ). The denser  $\mathbf{k}$  grids are used for the summations performed in Eq. (7), namely,  $300 \times 200 \times 1$  and  $200 \times 300 \times 1$  for *hr-sB* and  $8Pmnn$ , respectively. We include up to 30 electronic bands,  $\eta = 30$  meV for the broadening parameter, and the cutoff is 10 eV for the  $\mathbf{G}$  vectors. Notice we are convinced that ground-state properties (i.e., electronic band structure) obtained from the two separate DFT codes are practically identical.

### III. RESULTS AND DISCUSSION

#### A. Electronic structure and vibrational properties of borophene

In Fig. 1 we display the optimized structure and electronic bands along the high-symmetry points for the *hr-sB* and  $8Pmnn$  phases of borophene. The unit cells of both phases are rectangular and contain eight atoms. In contrast to the  $8Pmnn$  phase with buckled structure, the *hr-sB* phase is purely planar with stripes of hexagons and rhombs along the  $x$  axis [see Fig. 1(a)]. The boron atoms are called  $B_h$  and  $B_r$  in the hexagon and rhomb stripes, respectively. The  $8Pmnn$

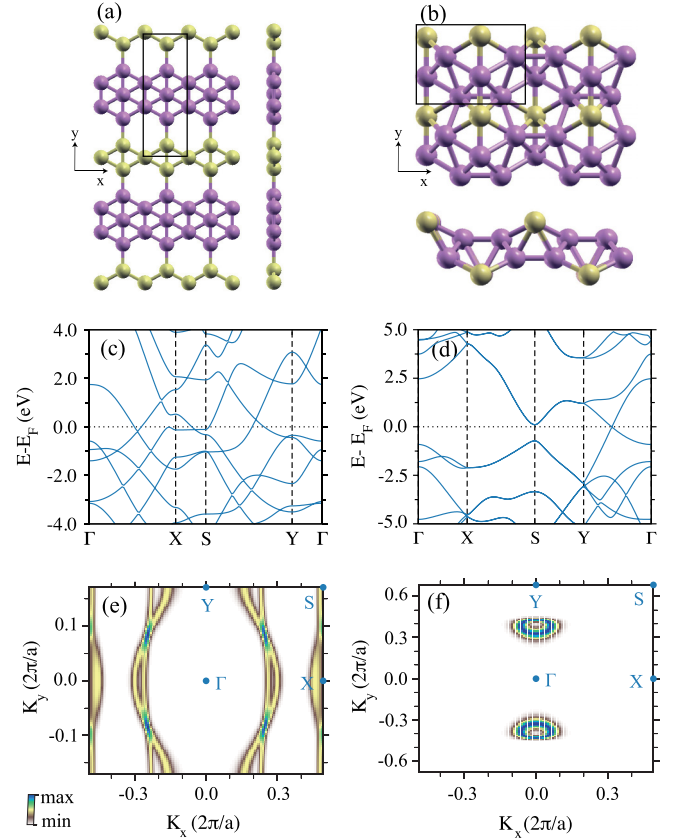


FIG. 1. Top and side views of optimized (a) *hr-sB* and (b)  $8Pmnn$  borophene structures. The primitive unit cell in both structures is marked by the black rectangle. The electronic band structure along the high-symmetry direction of *hr-sB* and  $8Pmnn$  are shown in (c) and (d), respectively. Panels (e) and (f) show the Fermi surfaces of a pristine *hr-sB* and hole-doped  $8Pmnn$  ( $E_F = -250$  meV). The boron atoms in the hexagon stripes ( $B_h$ ) (inner atoms  $B_I$ ) and in rhombus stripes ( $B_r$ ) (ridge atoms  $B_R$ ) are indicated in purple and yellow, respectively, in the *hr-sB* ( $8Pmnn$ ) phase.

borophene structure contains two types of nonequivalent B atoms, namely, the ridge atoms ( $B_R$ ) and the inner atoms ( $B_I$ ) [see Fig. 1(b)], leading to various physical and chemical properties. Figure 1(c) shows the anisotropic band structure of *hr-sB* with a Dirac nodal line and tilted semi-Dirac cones coexisting around the Fermi energy [38]. Two linear bands are crossed between the  $\Gamma$  and X points as well as between the S and Y points, forming Dirac points slightly below and above the Fermi level, respectively. These two structures are part of the Dirac nodal line, which can be seen from the Fermi-surface plot in Fig. 1(e). The tilted Dirac cone is at the edge of the Brillouin zone (BZ). The orthorhombic  $8Pmnn$  borophene possesses a tilted anisotropic Dirac cone along the  $\Gamma Y$  path, where the Dirac point crosses the Fermi level [see Fig. 1(d)] and the corresponding Fermi surface with  $E_F = -250$  meV in Fig. 1(f)]. It is worth mentioning that the Dirac cone of the  $8Pmnn$  borophene emerges from the symmetry of the hexagonal and topologically equivalent lattice to uniaxially strained graphene lattice [35].

In contrast to graphene where the two crossing linear bands both come from the  $p_z$  orbitals, in 2D boron allotropes the  $p_z$

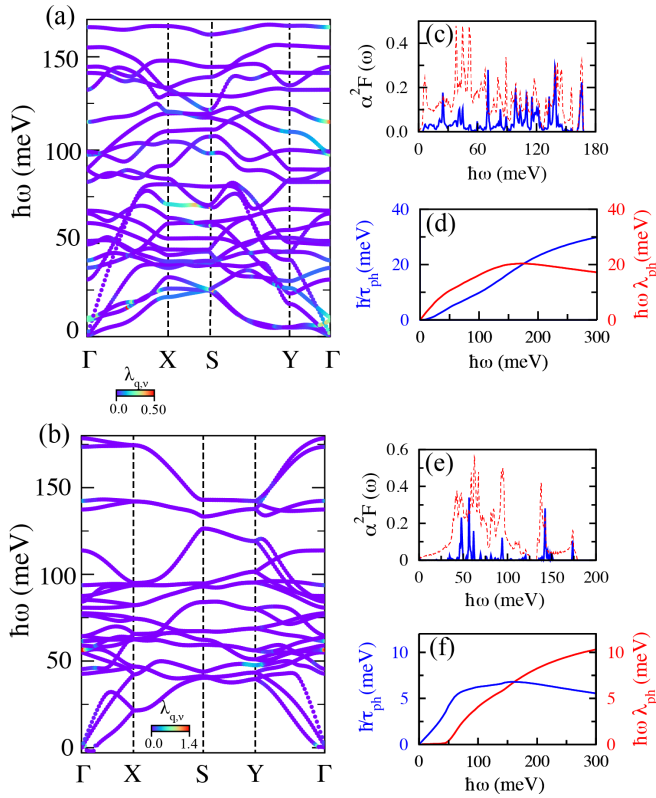


FIG. 2. The phonon band structure and momentum-resolved  $\lambda_{q,v}$  along the high-symmetry points for (a) pristine *hr-sB* and (b) hole-doped ( $E_F = -250$  meV) *8Pmnm* phases of borophene. The Eliashberg function  $\alpha^2F(\omega)$ , phonon-induced decay rate  $1/\tau_{ph}(\omega)$ , and energy renormalization parameter  $\omega\lambda_{ph}(\omega)$  for (c),(d) *hr-sB* and (e),(f) hole-doped *8Pmnm*. The phonon DOS for pristine *hr-sB* and hole-doped *8Pmnm* are indicated with red dashed lines.

orbitals are not the only dominating contribution to the Dirac cone. In the *hr-sB* sheet, the two crossing bands between the  $\Gamma$  and X points come from different orbitals originating in various atomic sites, i.e., the  $p_z$  orbitals of  $B_h$  atoms and the  $p_{x/y}$  orbitals of  $B_r$  atoms have dominating contributions. Along the XS direction, the  $p_z$  orbitals of both  $B_r$  and  $B_h$  atoms are contributing to the Dirac bands. Furthermore, the Dirac cones in *8Pmnm* are arising from the  $p_z$  orbitals of the  $B_l$  atoms with a much lesser contribution of the  $p_x$  orbitals. In this phase, the  $B_R$  atoms do not contribute to the formation of the electronic states in the vicinity of the Fermi level, which is in line with previous theoretical work [40].

The study of the EPC represents a fundamental and fascinating issue and it is the first step toward the calculations of the plasmon decay rates in the two phases of borophene. The dynamical matrices and phonon-perturbed potentials are calculated on a  $\Gamma$ -centered grid within the framework of DFPT. In Figs. 2(a) and 2(b), we show the phonon dispersions and momentum-resolved  $\lambda_{q,v}$  along the high-symmetry points (superimposed as a color code to the corresponding dispersions) and DOS for two chosen phases of borophene. Note that for the *8Pmnm* borophene, the hole-doped case with  $E_F = -250$  meV is considered. Such doping is regularly achieved in 2D materials, such as graphene, via the gate-tuning techniques [54], chemical dopings via intercalates or

adsorbates [48,55], as well as the presence of the dielectric or metallic substrate [56,57]. No imaginary vibrating mode is seen for the *hr-sB* phase of borophene, indicating the stability of this structure. In *8Pmnm* all the phonon modes are positive frequencies, except the transverse branch near the  $\Gamma$  point. Moreover, the results show that the EPC strength is remarkable along the XS direction and near the  $\Gamma$  point for *hr-sB*, while the EPC strength in *8Pmnm* is weak and appears for the modes at the  $\Gamma$  and Y points. The prominent peaks in the phonon DOS of *hr-sB* structure are located around 50, 90, and 150 meV and are due to the dispersionless nature of the phonon band structure around these energies. In the *8Pmnm* phase, the dispersionless phonon structures are also behind the peaks in the phonon DOS.

The Eliashberg function,  $\alpha^2F(\omega)$ , the phonon-induced decay rate  $1/\tau_{ph}(\omega)$ , and energy renormalization parameter  $\omega\lambda_{ph}(\omega)$  for the two phases of borophene are illustrated in Figs. 2(c)–2(f). The feature of the Eliashberg function for the *hr-sB* structure does not follow the phonon DOS for energies below 50 meV, but it resembles the phonon DOS above 50 meV. The most intense peaks come from the optical phonons near the  $\Gamma$  point and along the XS path, where momentum-resolved  $\lambda_{q,v}$  appears to be the strongest [see Fig. 2(a)]. Similarly, the characteristics of the Eliashberg function for *8Pmnm* are quite different from the ones shown in the phonon DOS and are mainly connected to the EPC strengths  $\lambda_{q,v}$  [Fig. 2(b)]. Regarding the total EPC strength, we have obtained the values of  $\lambda = 0.25$  and  $\lambda = 0.008$  for *hr-sB* and *8Pmnm* phases of borophene, respectively. Both of these values are smaller than what is reported for  $WTe_2$  ( $\lambda = 0.43$ ), which is another promising hyperbolic 2D material [14]. In hole-doped graphene with  $E_F = -250$  meV, the theoretically obtained EPC strength is  $\lambda = 0.018$  [58], which is still larger than what we obtain for the hole-doped *8Pmnm* borophene. It is surprising that the EPC in *8Pmnm* is extremely small and it is therefore expected that the corresponding phonon-induced plasmon decay is also quite small.

## B. Optical conductivity and hyperbolic regions

We now turn to the study of anisotropic optical properties in borophene. The appearance of hyperbolic regions for certain photon energy can be inspected by calculating the optical conductivity for different light polarization directions. The corresponding hyperbolic condition for specific photon energy  $\hbar\omega$  is defined as

$$\text{Im}[\sigma_x(\omega)] \times \text{Im}[\sigma_y(\omega)] < 0. \quad (10)$$

We display the imaginary (top) and the real (bottom) parts of optical conductivity along two principal axes for *hr-sB* (left) and *8Pmnm* (right) phases of borophene in Fig. 3. The hyperbolic regimes are depicted with the shaded area. The imaginary part of optical conductivity along the y axis for the *hr-sB* phase changes its sign around 1.0 eV and stays negative up to 1.58 eV. This demonstrates the first hyperbolic region in the *hr-sB* borophene. Interestingly, the second hyperbolic regime falls between 1.84 and 2.21 eV, i.e., in the visible range. The hyperbolicity condition for the *8Pmnm* phase of borophene is also met in the visible part of the spectrum, i.e., there is one small hyperbolic region around 1.66 eV and

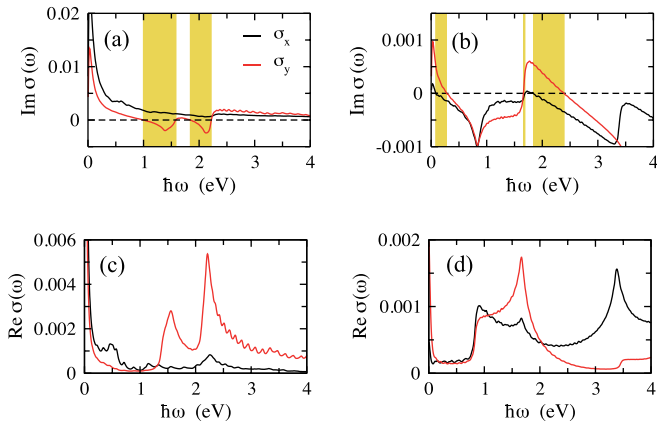


FIG. 3. The imaginary (top panel) and real parts (bottom panel) of the optical conductivity along the  $x$  (black line) and  $y$  (red line) directions for (a),(c)  $hr$ - $sB$  and (b),(d)  $8Pmmn$ . The shaded areas show the hyperbolic regions in both phases of borophene.

one with the energy window going from 1.85 to 2.39 eV. In addition, the  $8Pmmn$  borophene displays hyperbolic behavior also at the lower energies between 0.085 and 0.27 eV (mid-infrared).

From the results of the real parts of the optical conductivity, indicating the allowed intraband and interband optical transitions, one can examine the origin of these hyperbolic regions. For instance, in the  $hr$ - $sB$  phase, there are interband excitations between 1.5 and 2.5 eV, which are intense and allowed for the  $y$  direction while forbidden and negligible for the  $x$  direction. In the case of the  $8Pmmn$  phase, similar peaks are present for both directions, however, characterized with very different intensities. In addition, the  $8Pmmn$  phase has strongly anisotropic intraband transitions (see the Drude peaks for the  $x$  and  $y$  directions below 0.2 eV). All these results suggest an extremely promising hyperbolic optical property of these two phases of borophene.

We further inspect the optical absorption of  $hr$ - $sB$  that shows intense peaks due to interband transitions at energies below 3 eV, which can therefore interact with the Dirac plasmons. In Fig. 4 the real part of the interband optical conductivity  $\text{Re} \sigma_{\mu}^{\text{inter}}(\omega)$  is shown for particular interband transitions for  $x$  and  $y$  polarizations, coming from three valence bands (VB-2, VB-1, and VB) below and three conduction bands (CB, CB+1, and CB+2) above the Fermi level. The most intense absorption peaks in the presented energy range stem from the interband transitions from VB to CB, from VB to CB+1, as well as from VB-1 to CB. We single out three interband excitations relevant for the Dirac plasmon: (i) the prominent interband peak at  $\sim 0.5$  eV that is present for the  $\Gamma X$  direction, (ii) the absorption peak at  $\sim 1.5$  eV for the  $\Gamma Y$  direction, and (iii) the interband continuum that starts at  $\sim 1$  eV for the  $\Gamma X$  direction. According to Fig. 4(b), the interband peak (i) comes entirely from the VB to CB transitions around the X point of the BZ. The feature (ii) originates from interband transitions around the Y point including VB-1, VB, CB, and CB+1. The continuum (iii) is due to interband transitions between VB-2 and CB as well as between VB-1 and CB, both around the S point of the BZ.

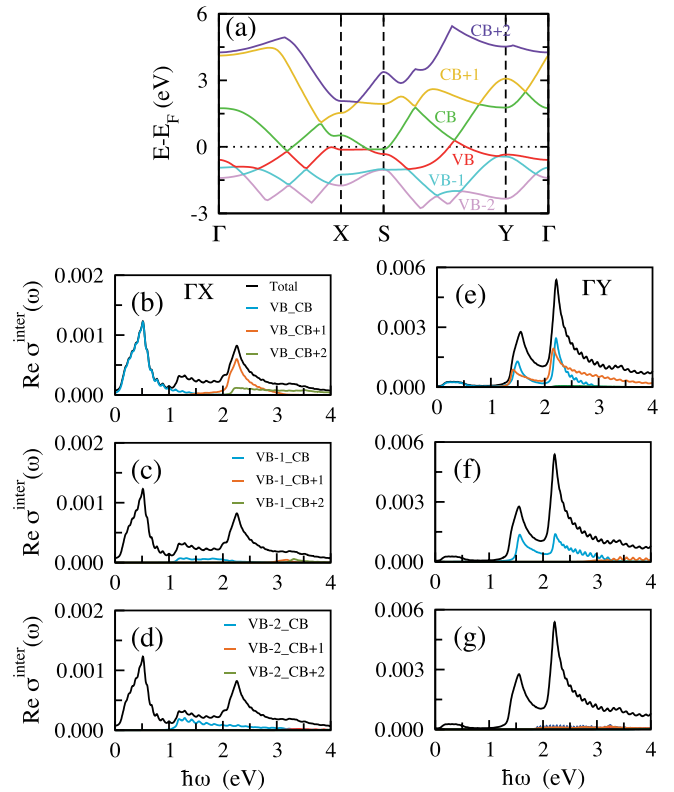


FIG. 4. (a) The electronic band structure of  $hr$ - $sB$  where three bands just below (VB-2, VB-1, and VB) and three bands just above the Fermi level (CB, CB+1, and CB+2) are illustrated with different colors. The different contributions to the interband optical absorption  $\text{Re} \sigma_{\mu}^{\text{inter}}(\omega)$  of  $hr$ - $sB$  coming from the transitions between the bands indicated in panel (a) when the polarization direction is along (b)–(d)  $\Gamma X$  and along (e)–(g)  $\Gamma Y$ . Total optical absorption is shown with the black line.

### C. Anisotropic dispersion and damping of Dirac plasmon

In this section, we first study the plasmon dispersion of the  $hr$ - $sB$  and  $8Pmmn$  phases of borophene in the optical limit (small  $\mathbf{q}$ ) for light polarization along the  $\Gamma X$  and  $\Gamma Y$  directions, where the electron-phonon interaction is included. To do so, we utilize the current-current (transverse) response formalism. We consider  $hr$ - $sB$  phase in the pristine (undoped) form; however, in the case of  $8Pmmn$ , the Fermi level is shifted 250 meV below the Dirac point to increase the carrier concentration. Figures 5(a) and 5(b) illustrate the plasmon dispersion of two phases of borophene along the two in-plane principal axes. The characteristics of the plasmon dispersion are very similar to the typical 2D Dirac semimetal in the long-wavelength limit, showing  $\sim \sqrt{q}$  dependence. However, there is a crucial difference here, namely, the very pronounced anisotropy in plasmon dispersion along the  $\Gamma X$  and  $\Gamma Y$  directions. This can be followed back to the strong anisotropy in the electronic structure [59] as well as to the anisotropy in the allowed optical (both intraband and interband) transitions along the two in-plane directions [as seen in Figs. 3(c) and 3(d)]. The similar behavior of 2D anisotropic plasmon dispersions has been reported in  $\text{WTe}_2$  [14] and black phosphorus [8,16,46,60]. It should be pointed out that such strong

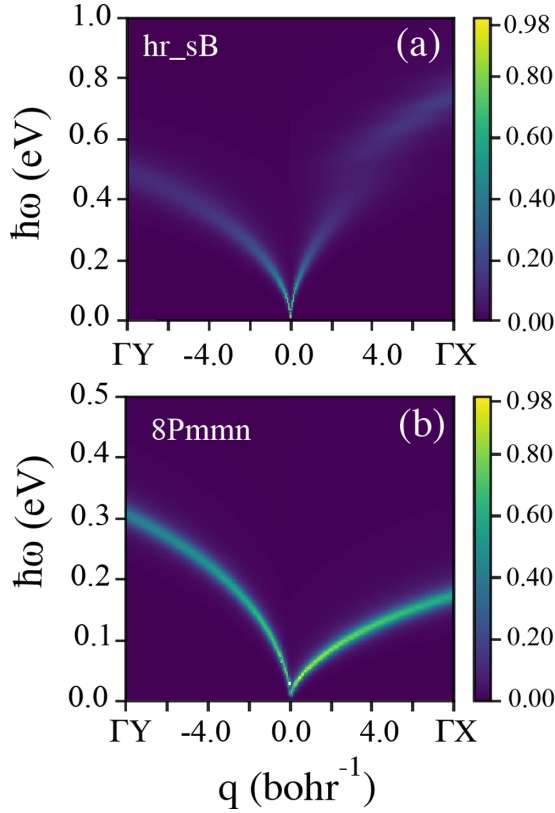


FIG. 5. Plasmon dispersions as a function of  $q$  (in  $10^{-3}$  bohr $^{-1}$ ) with incorporating the EPC at  $T = 0$  K for (a) pristine  $hr$ - $sB$  and (b) hole-doped  $8Pmmn$  ( $E_F = -250$  meV) phase of borophene along two principal axes, i.e.,  $\Gamma X$  and  $\Gamma Y$  directions.

anisotropy could lead to hyperbolic plasmons in 2D materials [14]. Therefore, the combination of a high anisotropy and strong metallic character could make both phases of borophene promising 2D hyperbolic materials.

In the following, we discuss the temperature dependence of the plasmon linewidth due to the EPC. Both phases of borophene are additionally compared with the prototypical Dirac material graphene with  $E_F = -250$  meV [58], as well as with the pristine  $WTe_2$  monolayer, which also supports hyperbolic plasmon modes [14]. The damping rates  $\hbar/\tau_{ph}$ , as a function of the temperature for two phases of borophene and graphene when  $\hbar\omega = 0.1$  eV and  $\hbar\omega = 0.2$  eV, are plotted in Figs. 6(a) and 6(b). Additionally, the damping rate for  $WTe_2$  when  $\hbar\omega = 0.1$  eV is shown in the Fig. 6(a). Compared with the  $8Pmmn$  borophene and graphene, the  $hr$ - $sB$  phase of borophene shows the largest damping rate due to the EPC and steepest temperature increase. Nevertheless, the EPC damping rate in the  $hr$ - $sB$  phase is still smaller than that in the  $WTe_2$  monolayer. For the presented plasmon energies, plasmon in graphene has the lowest damping rate. This is because under these conditions (i.e.,  $T \leq 300$  K and  $\hbar\omega \leq 0.2$  eV), graphene plasmon is only weakly coupled to acoustic phonons [58], while in both phases of borophene due to more complex structure, there are multiple low-energy optical and acoustic phonons that can couple to Dirac plasmon [see Fig. 2].

To perform a more thorough survey of plasmon damping, we calculate the total damping of plasmon that additionally

includes Landau damping (coupling to electron-hole pair transitions) by making use of the following expression [61],

$$\hbar\Gamma(\mathbf{q}, \omega) = 2\pi\hbar q \text{Re} \sigma_\mu(\mathbf{q}, \omega) \quad (11)$$

where  $\sigma_\mu(\mathbf{q}, \omega)$  contains both intraband  $\sigma_\mu^{\text{intra}}(\mathbf{q}, \omega)$  and interband  $\sigma_\mu^{\text{inter}}(\mathbf{q}, \omega)$  terms. The total damping for all three systems is illustrated in Figs. 6(c) and 6(d). For two phases of borophene,  $\hbar\Gamma(\mathbf{q}_{pl}, \omega_{pl})$  is plotted along the  $\Gamma X$  and  $\Gamma Y$  directions. As expected, the total damping in the  $hr$ - $sB$  phase of borophene is considerably larger than in the  $8Pmmn$  phase and graphene, because both EPC and interband transitions are stronger in  $hr$ - $sB$  [compare the intensities of  $\text{Re} \sigma_\mu$  in Figs. 3(c) and 3(d)]. Interestingly, the total plasmon damping of  $8Pmmn$  and graphene are remarkably similar at  $\hbar\omega_{pl} \leq 0.3$  eV. Furthermore, the total damping of Dirac plasmon in the  $hr$ - $sB$  phase shows a specific sharp increase at  $\sim 0.5$  eV, followed by a decrease, but only in the  $\Gamma X$  direction. This interesting feature comes from the above-mentioned interband feature (i) that is only allowed for the  $x$  polarization [compare  $\text{Re} \sigma_x(\omega)$  and  $\text{Re} \sigma_y(\omega)$  around 0.5 eV in Figs. 4(b) and 4(e)]. Note that this coupling between Dirac plasmon and interband transitions (i) also results in avoided crossing in plasmon dispersion along the  $\Gamma X$  direction, as observed in Figs. 5(a) and 6(e).

Figures 6(e)–6(g) show the plasmon dispersions of pristine  $hr$ - $sB$  as well as hole-doped  $8Pmmn$  and graphene ( $E_F = -250$  meV) along two principal axes at  $T = 300$  K. The temperature dependence of the plasmon energy comes from the Fermi-Dirac distribution function and also from the EPC through  $1/\tau_{ph}(\omega)$  and  $\lambda_{ph}(\omega)$  functions. The temperature dependence of the plasmon dispersion due to the EPC is remarkable for the  $hr$ - $sB$  borophene. On the other hand, the temperature dependence of the plasmon dispersion is weak in  $8Pmmn$  and graphene owing to the weak coupling of plasmon and phonons in these two materials. To have an insight into the temperature dependence of the plasmon, we illustrate the plasmon dispersions at  $T = 0$  K for  $hr$ - $sB$  and  $8Pmmn$  with the white dashed line in Figs. 6(e) and 6(f) respectively. For  $8Pmmn$ , it is obvious that the change in dispersion is negligible. On the other hand, it is considerable for  $hr$ - $sB$ , especially along the  $\Gamma X$  where it changes from 0.73 to 0.80 eV at largest  $q$  vector ( $8 \times 10^{-3}$  bohr $^{-1}$ ) when the temperature rises from  $T = 0$  K to  $T = 300$  K.

Overall, these results show an impressive anisotropy in borophene of both plasmon dispersion and plasmon damping along the  $\Gamma X$  and  $\Gamma Y$  directions. We would like to point out here that these anisotropic properties should not be altered significantly in the presence of the substrate, such as  $Ag(111)$ , or in the presence of the random disorder. According to Refs. [30,62], the electronic structure and plasmonic response of borophene is altered due to the proximity of the metallic substrate; however, the corresponding anisotropy is preserved since the dielectric screening of the substrate is isotropic. We further expect that the plasmon modes would be confined vertically and as a consequence slow down the plasmon velocity when the system is placed nearby a metal [63]. Furthermore, the substrate effects might be reduced by the intercalation of other atoms between 2D material and the surface, which partially recovers the free-standing nature of the adsorbed

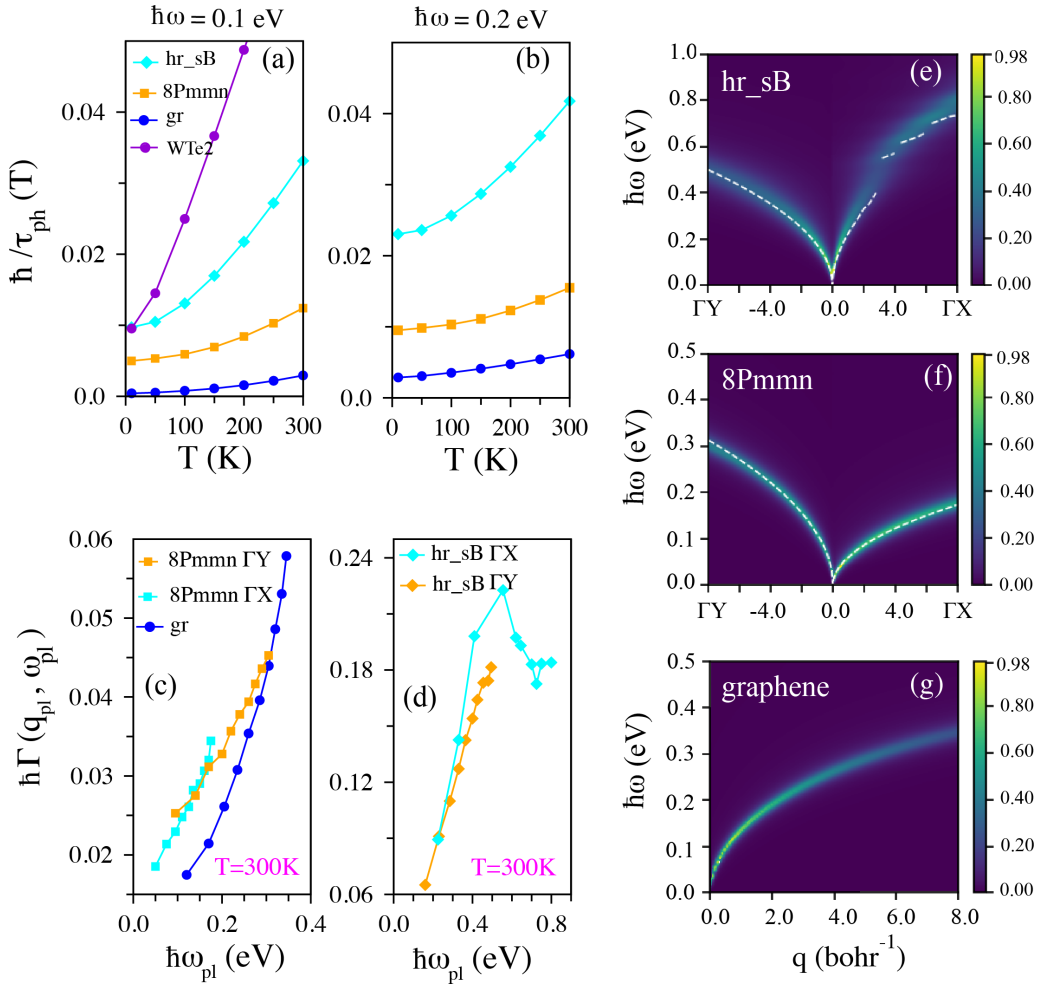


FIG. 6. Plasmon damping rates owing to the EPC  $\hbar/\tau_{\text{ph}}(\omega)$  as a function of the temperature for *hr-sB*, *8Pmmn*, and graphene when energy is (a)  $\hbar\omega = 0.1$  eV and (b)  $\hbar\omega = 0.2$  eV. The corresponding damping rate for the *WTe<sub>2</sub>* monolayer is shown for comparison as well [14], where  $\hbar/\tau_{\text{ph}} = 73$  meV for  $T = 300$  K (not shown). Total damping of plasmon which additionally includes Landau damping along the  $x$  and  $y$  directions and  $T = 300$  K for (c) graphene and *8Pmmn* ( $E_{\text{F}} = -250$  meV) as well as for (d) *hr-sB*. Plasmon dispersions of (e) *hr-sB*, (f) *8Pmmn*, and (g) graphene as a function of  $q$  (in  $10^{-3}$  bohr<sup>-1</sup>) when the EPC is included at  $T = 300$  K. The white dashed lines in (e) and (f) show the plasmon dispersions at  $T = 0$  K for *hr-sB* and *8Pmmn*, respectively.

layers [64,65]. As for the impact of disorder, due to its random distribution, it is expected to introduce an additional broadening [66,67], but not to alter the anisotropic properties of borophene. In addition, we examine the anisotropic electron excitons in the two phases of borophene in the short-wavelength regime (finite  $\mathbf{q}$ ). To provide a dispersion relation of the plasmon modes in borophene when  $\mathbf{q} > 0$ , we calculate the charge-charge response function and the corresponding dielectric function  $\varepsilon(\mathbf{q}, \omega)$  [68–70]. The electron energy loss function  $\text{Im}[1/\varepsilon(\mathbf{q}, \omega)]$  for two phases of borophene is illustrated in Figs. 7(a) and 7(b) for  $q \leq 0.06$  bohr<sup>-1</sup> and  $\omega \leq 4.0$  eV. Note that for the smallest momentum the Dirac plasmon dispersion obtained by the charge-charge (longitudinal) response formalism is in good agreement with the results obtained by means of the current-current (transverse) response theory. For larger momenta, the remarkable anisotropy of Dirac plasmon in borophene is even more pronounced, especially for the *hr-sB* phase, where plasmons energies, for instance, at  $q = 0.06$  bohr<sup>-1</sup> are  $\hbar\omega_{\text{pl}} \approx 2$  eV and  $\hbar\omega_{\text{pl}} \approx 0.8$  eV along the  $\Gamma X$  and  $\Gamma Y$  directions, respectively. Also,

the plasmon energy in the *hr-sB* phase reaches the visible range along the  $\Gamma X$  direction due to intrinsic high carrier density as well as the low intensity of interband transitions (and therefore minor interband screening) for the  $x$  polarization [see Fig. 3(c)]. Relevant low intensity interband transitions are here interband continuum (iii) at around 1 eV discussed above [see Figs. 4(c) and 4(d)]. On the other hand, a strong interband feature (ii) at around 1.5 eV screens and pushes the Dirac plasmon to lower energies for the  $y$  polarization. For both phases of borophene, the interband screening makes the Dirac plasmon dispersionless and most importantly flat. This makes the group velocity of plasmon small, which might be important in the context of real-space localization of plasmon wave packets [71]. Apart from the Dirac plasmons, here we can perceive the presence of the anisotropic screened interband excitations (i.e., interband plasmons). Particularly interesting are the interband excitations in the *8Pmmn* phase that fall into the visible range due to their high intensity and anisotropy. In addition, an acoustic plasmon is present in the *8Pmmn* phase and it comes from the anisotropic Fermi velocity along

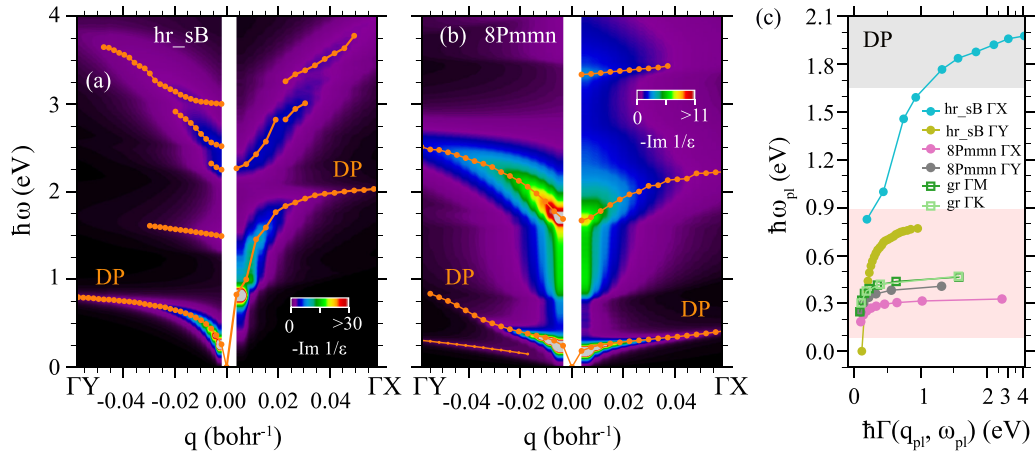


FIG. 7. The electron energy loss function  $\text{Im}[1/\epsilon(\mathbf{q}, \omega)]$  as a function of energy  $\hbar\omega$  and momentum  $q$  along the  $\Gamma X$  and  $\Gamma Y$  directions for (a) the pristine  $hr\text{-}sB$  and (b) the  $8Pmnm$  ( $E_F = -250$  meV) borophene. The orange dots follow the plasmon peaks in these two systems. Both phases show strongly anisotropic Dirac plasmon (DP) mode. (c) The total damping for two phases of borophene and graphene as a function of plasmon frequency  $\hbar\omega_{pl}$  and along the corresponding high-symmetry directions. The mid-infrared and visible regions are highlighted with the red- and gray-shaded areas, respectively.

two principal directions (i.e., the anisotropic Dirac cone) [72].

Ultimately, we inspect the total plasmon damping for  $\mathbf{q} > 0$ , which is shown in Fig. 7(c). It turns out that in the  $hr\text{-}sB$  phase, the Dirac plasmon along the  $\Gamma X$  direction is strongly damped for energies in the visible range (i.e.,  $\hbar\Gamma > 1$  eV). The corresponding plasmon along the  $\Gamma Y$  direction, which falls into the mid-infrared region, is, on the other hand, moderately damped. In accordance with our conclusions for the plasmon damping in the long-wavelength limit, the plasmon decay rates of the hole-doped  $8Pmnm$  borophene and graphene are similar. The unique considerable difference is the anisotropy of plasmon damping for the  $8Pmnm$  borophene.

#### IV. CONCLUSION

By using the DFT-based calculations, we have examined optical properties and collective electron excitation modes (i.e., plasmons) in two phases of single-layer boron (borophene) that host Dirac fermions with tilted Dirac cone, namely, the so-called  $hr\text{-}sB$  and  $8Pmnm$  borophene. According to our numerical results, both of these phases are dynamically stable and are characterized with a strongly anisotropic electronic structure and optical absorption. In fact, hyperbolic plasmonic surfaces appear in the visible range. The

$hr\text{-}sB$  phase, with tilted Dirac cone and nodal line, supports strong hyperbolic Dirac plasmons already in the pristine form owing to the excessive concentration of carriers at the Fermi energy. The  $8Pmnm$  borophene is a semimetal with Dirac point crossing the Fermi level and therefore supports plasmon modes only on carrier doping. For the hole-doped  $8Pmnm$  phase, we have determined hyperbolic Dirac plasmons in the mid-infrared region. By analyzing the coupling of Dirac plasmon with phonons and electron-hole pair excitations, we show that the  $8Pmnm$  phase has a very low plasmonic damping rate.

Both of these phases of borophene outperform typical 2D Dirac material, i.e., graphene, as an optical and plasmonic device owing to intrinsic metallic character, strong anisotropy, the appearance of hyperbolic plasmonic surfaces, low plasmon losses, and plasmons in the visible range.

#### ACKNOWLEDGMENTS

D.N. acknowledges financial support from the Croatian Science Foundation (Grant No. UIP-2019-04-6869) and from the European Regional Development Fund for the ‘‘Center of Excellence for Advanced Materials and Sensing Devices’’ (Grant No. KK.01.1.1.01.0001). R.A. was supported by the Australian Research Council Centre of Excellence in Future Low-Energy Electronics Technologies (Project No. CE170100039).

- [1] A. Poddubny, I. Iorsh, P. Belov, and Y. Kivshar, Hyperbolic metamaterials, *Nat. Photonics* **7**, 948 (2013).
- [2] J. Sun, N. M. Litchinitser, and Ji Zhou, Indefinite by nature: From ultraviolet to terahertz, *ACS Photonics* **1**, 293 (2014).
- [3] M. N. Gjerding, R. Petersen, T. G. Pedersen, N. A. Mortensen, and K. S. Thygesen, Layered van der waals crystals with hyperbolic light dispersion, *Nat. Commun.* **8**, 320 (2017).
- [4] S. Biswas, W. S. Whitney, M. Y. Grajower, K. Watanabe, T. Taniguchi, H. A. Bechtel, G. R. Rossman, and H. A. Atwater, Tunable intraband optical conductivity and polarization-

dependent epsilon-near-zero behavior in black phosphorus, *Sci. Adv.* **7**, eabd4623 (2021).

- [5] M. He, S. I. Halimi, T. G. Folland, S. S. Sunku, S. Liu, J. H. Edgar, D. N. Basov, S. M. Weiss, and J. D. Caldwell, Guided mid-IR and near-IR light within a hybrid hyperbolic-material/silicon waveguide heterostructure, *Adv. Mater.* **33**, 2004305 (2021).
- [6] W. T. Chen, A. Y. Zhu, and F. Capasso, Flat optics with dispersion-engineered metasurfaces, *Nat. Rev. Mater.* **5**, 604 (2020).

- [7] J. D. Caldwell, A. V. Kretinin, Y. Chen, V. Giannini, M. M. Fogler, Y. Francescato, C. T. Ellis, J. G. Tischler, C. R. Woods, A. J. Giles *et al.*, Sub-diffractive volume-confined polaritons in the natural hyperbolic material hexagonal boron nitride, *Nat. Commun.* **5**, 1 (2014).
- [8] J. S. Gomez-Diaz and A. Alù, Flatland optics with hyperbolic metasurfaces, *ACS Photonics* **3**, 2211 (2016).
- [9] W. Ma, P. Alonso-González, S. Li, A. Y. Nikitin, J. Yuan, J. Martín-Sánchez, J. Taboada-Gutiérrez, I. Amenabar, P. Li, S. Vélez, C. Tollan, Z. Dai, Y. Zhang, S. Sriram, K. Kalantar-Zadeh, S.-T. Lee, R. Hillenbrand, and Q. Bao, In-plane anisotropic and ultra-low-loss polaritons in a natural van der Waals crystal, *Nature (London)* **562**, 557 (2018).
- [10] T. Low, A. Chaves, J. D. Caldwell, A. Kumar, N. X. Fang, P. Avouris, T. F. Heinz, F. Guinea, L. Martin-Moreno, and F. Koppens, Polaritons in layered two-dimensional materials, *Nat. Mater.* **16**, 182 (2016).
- [11] D. N. Basov, A. Asenjo-Garcia, P. J. Schuck, X. Zhu, and A. Rubio, Polariton panorama, *Nanophotonics* **10**, 549 (2021).
- [12] C. Wang, S. Huang, Q. Xing, Y. Xie, C. Song, F. Wang, and H. Yan, Van der Waals thin films of WTe<sub>2</sub> for natural hyperbolic plasmonic surfaces, *Nat. Commun.* **11**, 1158 (2020).
- [13] C. Wang, Y. Sun, S. Huang, Q. Xing, G. Zhang, C. Song, F. Wang, Y. Xie, Y. Lei, Z. Sun, and H. Yan, Tunable Plasmons in Large-Area WTe<sub>2</sub> Thin Films, *Phys. Rev. Applied* **15**, 014010 (2021).
- [14] Z. Torbatian, D. Novko, and R. Asgari, Tunable Low-Loss Hyperbolic Plasmon Polaritons in a T<sub>d</sub>-WTe<sub>2</sub> Single Layer, *Phys. Rev. Appl.* **14**, 044014 (2020).
- [15] D. Correias-Serrano, J. S. Gomez-Diaz, A. A. Melcon, and A. Alù, Black phosphorus plasmonics: Anisotropic elliptical propagation and nonlocality-induced canalization, *J. Opt.* **18**, 104006 (2016).
- [16] E. van Veen, A. Nemilentsau, A. Kumar, R. Roldán, M. I. Katsnelson, T. Low, and S. Yuan, Tuning Two-Dimensional Hyperbolic Plasmons in Black Phosphorus, *Phys. Rev. Applied* **12**, 014011 (2019).
- [17] S. Guan, S. Y. Huang, Y. Yao, and S. A. Yang, Tunable hyperbolic dispersion and negative refraction in natural electride materials, *Phys. Rev. B* **95**, 165436 (2017).
- [18] H. Wang and T. Low, Hyperbolicity in two-dimensional transition metal ditellurides induced by electronic bands nesting, *Phys. Rev. B* **102**, 241104(R) (2020).
- [19] S. Edalati-Boostan, C. Cocchi, and C. Draxl, MoTe<sub>2</sub> as a natural hyperbolic material across the visible and the ultraviolet region, *Phys. Rev. Mater.* **4**, 085202 (2020).
- [20] A. Ebrahimi and R. Asgari, Natural hyperbolicity in layered hexagonal crystal structures, *Phys. Rev. B* **103**, 035425 (2021).
- [21] J. Zhao, W. Wu, J. Zhu, Y. Lu, B. Xiang, and S. A. Yang, Highly anisotropic two-dimensional metal in monolayer MoOCl<sub>2</sub>, *Phys. Rev. B* **102**, 245419 (2020).
- [22] Y. Huang, S. N. Shirodkar, and B. I. Yakobson, Two-dimensional boron polymorphs for visible range plasmonics: A first-principles exploration, *J. Am. Chem. Soc.* **139**, 17181 (2017).
- [23] Z. Xie, X. Meng, X. Li, W. Liang, W. Huang, K. Chen, J. Chen, C. Xing, M. Qiu, B. Zhang *et al.*, Two-dimensional borophene: Properties, fabrication, and promising applications, *Research* **2020**, 2624617 (2020).
- [24] L. Yan, P.-F. Liu, H. Li, Y. Tang, J. He, X. Huang, B.-T. Wang, and L. Zhou, Theoretical dissection of superconductivity in two-dimensional honeycomb borophene oxide B<sub>2</sub>O crystal with a high stability, *npj Comput. Mater.* **6**, 1 (2020).
- [25] C. Hou, G. Tai, Z. Wu, and J. Hao, Borophene: Current status, challenges and opportunities, *ChemPlusChem* **85**, 2186 (2020).
- [26] S. I. Vishkayi and M. B. Tagani, Current-voltage characteristics of borophene and borophane sheets, *Phys. Chem. Chem. Phys.* **19**, 21461 (2017).
- [27] M. Gao, Q.-Z. Li, X.-W. Yan, and J. Wang, Prediction of phonon-mediated superconductivity in borophene, *Phys. Rev. B* **95**, 024505 (2017).
- [28] L. Adamska, S. Sadasivam, J. J. Foley, P. Darancet, and S. Sharifzadeh, First-principles investigation of borophene as a monolayer transparent conductor, *J. Phys. Chem. C* **122**, 4037 (2018).
- [29] C. Lian, S.-Q. Hu, J. Zhang, C. Cheng, Z. Yuan, S. Gao, and S. Meng, Integrated Plasmonics: Broadband Dirac Plasmons in Borophene, *Phys. Rev. Lett.* **125**, 116802 (2020).
- [30] A. Haldar, C. L. Cortes, P. Darancet, and S. Sharifzadeh, Microscopic theory of plasmons in substrate-supported borophene, *Nano Lett.* **20**, 2986 (2020).
- [31] S. A. Dereshgi, Z. Liu, and K. Aydin, Anisotropic localized surface plasmons in borophene, *Opt. Express* **28**, 16725 (2020).
- [32] A. J. Mannix, X.-F. Zhou, B. Kiraly, J. D. Wood, D. Alducin, B. D. Myers, X. Liu, B. L. Fisher, U. Santiago, J. R. Guest *et al.*, Synthesis of borophenes: Anisotropic, two-dimensional boron polymorphs, *Science* **350**, 1513 (2015).
- [33] B. Feng, J. Zhang, Q. Zhong, W. Li, S. Li, H. Li, P. Cheng, S. Meng, L. Chen, and K. Wu, Experimental realization of two-dimensional boron sheets, *Nat. Chem.* **8**, 563 (2016).
- [34] X.-F. Zhou, X. Dong, A. R. Oganov, Q. Zhu, Y. Tian, and H.-T. Wang, Semimetallic Two-Dimensional Boron Allotrope with Massless Dirac Fermions, *Phys. Rev. Lett.* **112**, 085502 (2014).
- [35] A. Lopez-Bezanilla and P. B. Littlewood, Electronic properties of 8-*pmmn* borophene, *Phys. Rev. B* **93**, 241405(R) (2016).
- [36] S. Verma, A. Mawrie, and T. K. Ghosh, Effect of electron-hole asymmetry on optical conductivity in 8-*pmmn* borophene, *Phys. Rev. B* **96**, 155418 (2017).
- [37] K. Sadhukhan and A. Agarwal, Anisotropic plasmons, Friedel oscillations, and screening in 8-*Pmmn* borophene, *Phys. Rev. B* **96**, 035410 (2017).
- [38] B. Feng, O. Sugino, Ro-Ya Liu, J. Zhang, R. Yukawa, M. Kawamura, T. Iimori, H. Kim, Y. Hasegawa, H. Li *et al.*, Dirac Fermions in Borophene, *Phys. Rev. Lett.* **118**, 096401 (2017).
- [39] K. M. Omambac, M. Petrović, P. Bampoulis, C. Brand, M. A. Kriegel, P. Dreher, D. Janoschka, U. Hagemann, N. Hartmann, P. Valerius, T. Michely, F. J. Meyer zu Heringdorf, and M. Horn-von Hoegen, Segregation-enhanced epitaxy of borophene on Ir(111) by thermal decomposition of borazine, *ACS Nano* **15**, 7421 (2021).
- [40] H. Zhang, Y. Xie, Z. Zhang, C. Zhong, Y. Li, Z. Chen, and Y. Chen, Dirac nodal lines and tilted semi-dirac cones coexisting in a striped boron sheet, *J. Phys. Chem. Lett.* **8**, 1707 (2017).
- [41] P. Giannozzi, S. Baroni, N. Bonini, M. Calandra, R. Car, C. Cavazzoni, D. Ceresoli, G. L. Chiarotti, M. Cococcioni, I. Dabo, A. D. Corso, S. de Gironcoli, S. Fabris, G. Fratesi, R. Gebauer, U. Gerstmann, C. Gougoussis, A. Kokalj, M. Lazzeri, L. Martin-Samos *et al.*, Quantum espresso: a modular and open-

- source software project for quantum simulations of materials, *J. Phys. Condens. Matter* **21**, 395502 (2009).
- [42] A. A. Mostofi, J. R. Yates, Y.-S. Lee, I. Souza, D. Vanderbilt, and N. Marzari, wannier90: A tool for obtaining maximally localised Wannier functions, *Comput. Phys. Commun.* **178**, 685 (2008).
- [43] S. Ponc e, E. R. Margine, C. Verdi, and F. Giustino, Epw: Electron-phonon coupling, transport and superconducting properties using maximally localized wannier functions, *Comput. Phys. Commun.* **209**, 116 (2016).
- [44] S. Baroni, S. de Gironcoli, A. Dal Corso, and P. Giannozzi, Phonons and related crystal properties from density-functional perturbation theory, *Rev. Mod. Phys.* **73**, 515 (2001).
- [45] D. Novko, M.  Sunji c, and V. Despoja, Optical absorption and conductivity in quasi-two-dimensional crystals from first principles: Application to graphene, *Phys. Rev. B* **93**, 125413 (2016).
- [46] Z. Torbatian and R. Asgari, Optical absorption properties of few-layer phosphorene, *Phys. Rev. B* **98**, 205407 (2018).
- [47] Z. Torbatian, M. Alidoosti, D. Novko, and R. Asgari, Low-loss two-dimensional Plasmon modes in antimonene, *Phys. Rev. B* **101**, 205412 (2020).
- [48] D. Novko, Dopant-induced plasmon decay in graphene, *Nano Lett.* **17**, 6991 (2017).
- [49] F. Caruso, D. Novko, and C. Draxl, Phonon-assisted damping of plasmons in three- and two-dimensional metals, *Phys. Rev. B* **97**, 205118 (2018).
- [50] P. B. Allen, Electron-phonon effects in the infrared properties of metals, *Phys. Rev. B* **3**, 305 (1971).
- [51] D. Novko, Broken adiabaticity induced by Lifshitz transition in MoS<sub>2</sub> and WS<sub>2</sub> single layers, *Communications Physics* **3**, 1 (2020).
- [52] D. Novko, Nonadiabatic coupling effects in MgB<sub>2</sub> reexamined, *Phys. Rev. B* **98**, 041112(R) (2018).
- [53] J. Enkovaara, C. Rostgaard, J. J. Mortensen, J. Chen, M. Du lak, L. Ferrighi, J. Gavnholt, C. Glinsvad, V. Haikola, H. A. Hansen, H. H. Kristoffersen, M. Kuisma, A. H. Larsen, L. Lehtovaara, M. Ljungberg, O. Lopez-Acevedo, P. G. Moses, J. Ojanen, T. Olsen, V. Petzold *et al.*, Electronic structure calculations with GPAW: A real-space implementation of the projector augmented-wave method, *J. Phys. Condens. Matter* **22**, 253202 (2010).
- [54] Z. Q. Li, E. A. Henriksen, Z. Jiang, Z. Hao, M. C. Martin, P. Kim, H. L. Stormer, and D. N. Basov, Dirac charge dynamics in graphene by infrared spectroscopy, *Nat. Phys.* **4**, 532 (2008).
- [55] A. V. Fedorov, N. I. Verbitskiy, D. Haberer, C. Struzzi, L. Petaccia, D. Usachov, O. Y. Vilkov, D. V. Vyalikh, J. Fink, M. Knupfer, B. B uchner, and A. Gr uneis, Observation of a universal donor-dependent vibrational mode in graphene, *Nat. Commun.* **5**, 3257 (2014).
- [56] F. Varchon, R. Feng, J. Hass, X. Li, B. Ngoc Nguyen, C. Naud, P. Mallet, J. Y. Veillen, C. Berger, E. H. Conrad, and L. Magaud, Electronic Structure of Epitaxial Graphene Layers on Sic: Effect of the Substrate, *Phys. Rev. Lett.* **99**, 126805 (2007).
- [57] S. Mammadov, J. Ristein, R. J. Koch, M. Ostler, C. Raidel, M. Wanke, R. Vasiliauskas, R. Yakimova, and T. Seyller, Polarization doping of graphene on silicon carbide, *2D Materials* **1**, 035003 (2014).
- [58] D. Novko, First-principles study of ultrafast dynamics of dirac plasmon in graphene, *New J. Phys.* **23**, 043023 (2021).
- [59] R. Hayn, Te Wei, V. M. Silkin, and J. van den Brink, Plasmons in anisotropic Dirac systems, *Phys. Rev. Mater.* **5**, 024201 (2021).
- [60] F. G. Ghamsari and R. Asgari, Plasmon-phonon-polaritons in encapsulated phosphorene, *Plasmonics* **15**, 1289 (2020).
- [61] I. Kup ci c, Damping effects in doped graphene: The relaxation-time approximation, *Phys. Rev. B* **90**, 205426 (2014).
- [62] J. C. Alvarez-Quiceno, G. R. Schleder, E. Marinho, and A. Fazzio, Adsorption of 3d, 4d, and 5d transition metal atoms on  $\beta_{12}$ —borophene, *J. Phys. Condens. Matter* **29**, 305302 (2017).
- [63] M. B. Lundberg, Y. Gao, R. Asgari, C. Tan, B. Van Duppen, M. Autore, P. Alonso-Gonz alez, A. Woessner, K. Watanabe, T. Taniguchi *et al.*, Tuning quantum nonlocal effects in graphene plasmonics, *Science* **357**, 187 (2017).
- [64] C. Riedl, C. Coletti, T. Iwasaki, A. A. Zakharov, and U. Starke, Quasi-Free-Standing Epitaxial Graphene on Sic Obtained by Hydrogen Intercalation, *Phys. Rev. Lett.* **103**, 246804 (2009).
- [65] J. C. Kotsakidis, A. Grubi ci c- Cabo, Y. Yin, A. Tadich, R. L. Myers-Ward, M. DeJarld, S. P. Pavunny, M. Currie, K. M. Daniels, C. Liu, M. T. Edmonds, N. V. Medhekar, D. K. Gaskill, A. L. V azquez de Parga, and M. S. Fuhrer, Freestanding n-doped graphene via intercalation of calcium and magnesium into the buffer LayerSiC(0001) interface, *Chem. Mater.* **32**, 6464 (2020).
- [66] A. Principi, G. Vignale, M. Carrega, and M. Polini, Impact of disorder on dirac plasmon losses, *Phys. Rev. B* **88**, 121405(R) (2013).
- [67] G. Viola, T. Wenger, J. Kinaret, and M. Fogelstr om, Graphene plasmons: Impurities and nonlocal effects, *Phys. Rev. B* **97**, 085429 (2018).
- [68] V. Despoja, D. Novko, K. Dekani c, M.  Sunji c, and L. Maru si c, Two-dimensional and  $\pi$  plasmon spectra in pristine and doped graphene, *Phys. Rev. B* **87**, 075447 (2013).
- [69] Z. Torbatian and R. Asgari, Plasmon modes of bilayer molybdenum disulfide: A density functional study, *J. Phys. Condens. Matter* **29**, 465701 (2017).
- [70] Z. Torbatian and R. Asgari, Plasmonic physics of 2d crystalline materials, *Applied Sciences* **8**, 238 (2018).
- [71] F. H. da Jornada, L. Xian, A. Rubio, and S. G. Louie, Universal slow plasmons and giant field enhancement in atomically thin quasi-two-dimensional metals, *Nat. Commun.* **11**, 1013 (2020).
- [72] M. Pizarra, A. Sindona, P. Riccardi, V. M. Silkin, and J. M. Pitarke, Acoustic plasmons in extrinsic free-standing graphene, *New J. Phys.* **16**, 083003 (2014).